The Astrophysical Journal, 718:1036–1045, 2010 August 1 doi:10.1088/0004-637X/718/2/1036

SPITZER, VERY LARGE TELESCOPE, AND VERY LARGE ARRAY OBSERVATIONS OF THE GALACTIC LUMINOUS BLUE VARIABLE CANDIDATE HD 168625

G. Umana[1], C. S. Buemi[1], C. Trigilio[1], P. Leto[1], and J. L. Hora[2]
[1] INAF-Osservatorio Astrofisico di Catania, Via S. Sofia 78, 95123 Catania, Italy
[2] Harvard-Smithsonian Center for Astrophysics, 60 Garden St. MS-65, Cambridge, MA 02138-1516, USA
Received 2009 November 18; accepted 2010 June 4; published 2010 July 12

ABSTRACT

We present mid-IR and radio observations of the Galactic luminous blue variables (LBVs) candidate HD 168625 and its associated nebula. We obtained mid-IR spectroscopic observations using the Infrared Spectrograph on board the *Spitzer Space Telescope*, and performed mid-IR and radio imaging observations using VISIR on the Very Large Telescope and the Very Large Array with comparable angular resolution. Our spectroscopic observations detected spectral features attributable to polycyclic aromatic hydrocarbons (PAHs) and therefore indicate the presence of a photodissociation region (PDR) around the ionized nebula. This result increases the number of LBVs and LBV candidates where a PDR has been found, confirming the importance of such a component in the total mass-loss budget of the central object during this elusive phase of massive star evolution. We have analyzed and compared the mid-IR and radio maps, and derive several results concerning the associated nebula. There is evidence for grain distribution variations across the nebula, with a predominant contribution from bigger grains in the northern part of the nebula while PAH and smaller grains are more concentrated in the southern part. A compact radio component located where there is a lack of thermal dust grains corroborates the presence of a shock in the southern nebula, which could arise as a consequence of the interaction of a fast outflow with the slower, expanding dusty nebula. Such a shock would be a viable means for PAH production as well as for changes in the grain size distribution. Finally, from the detection of a central radio component probably associated with the wind from the central massive supergiant, we derive a current mass-loss rate of $\dot{M} = (1.46 \pm 0.15) \times 10^{-6}\, M_{\odot}\, \mathrm{yr}^{-1}$.

Key words: circumstellar matter – infrared: stars – stars: early-type – stars: individual (HD 168625) – stars: winds, outflows

1. INTRODUCTION

The post-main-sequence (MS) evolution of massive stars is still far from being clearly understood. Massive stars lose most of their initial mass as they follow the path from the MS toward the Wolf–Rayet (W-R) phase, and this severe mass loss probably occurs through stellar winds and/or eruptions. Luminous blue variables (LBVs) may play a key role in this scenario. LBVs are thought to be stars in a brief ($\sim 10^5$ yr) hot supergiant phase, characterized by strong spectral and photometric variability and high mass-loss rates (10^{-5}–$10^{-4}\, M_{\odot}\, \mathrm{yr}^{-1}$; van Genderen 2001; Davies et al. 2005). More rarely, LBVs undergo giant eruptions in which massive circumstellar nebulae (LBVNs) of up to a few $M_{\odot}$ are ejected, and whose presence is revealed by nebular emission lines and excess IR emission (Clark et al. 2005). The possibility that such spectacular mass-loss events may be metallicity independent has greatly increased the interest in LBVs, as this can have important implications for the mass loss, and therefore the evolution, of Population III stars (Smith & Owocki 2006).

There are still many open questions about the LBV phenomenon, including the origin and modality of mass-loss episodes, and the formation and shaping of the resulting nebulae, which quite often exhibit a bipolar morphology (Weis 2008). Some authors, based on broad similarities between the observed bipolar morphologies of LBVN and planetary nebulae, propose that similar physical agents act to shape these objects (i.e., a dusty disk or in general a strong unbalanced density in the nebula; Nota et al. 1995; O'Hara et al. 2003). However, it is unclear whether the asymmetric morphologies of some LBV ejecta are due to a pre-existing density contrast or if the wind itself is asymmetric (Frank et al. 1998; Maeder et al. 2005). Several LBVs have been found by *IRAS*, the *Infrared Space Observatory*, *Midcourse Space Experiment*, and ground-based near-IR and mid-IR imaging to have spatially resolved shells (Clark et al. 2003). Evidence of departures from spherical symmetry has been seen, but the resolution of these previous observations has not been sufficient to show the detailed structure of the shells and therefore cannot differentiate between the possible shaping mechanisms.

A better understanding of the mechanisms responsible for the formation and shaping of LBVNs requires high-resolution, multi-wavelength images to trace the different emitting components coexisting in the stellar ejecta: the ionized/neutral gas and the dust. A detailed knowledge of the gas and dust distribution would allow us to evaluate the total mass of the nebula and identify the presence of multiple shells related to different mass-loss episodes, and thus examine the total mass lost by the central object during this critical evolutionary phase. More importantly, it would provide observational evidence of possible mutual interaction between the gas and dust components and provide a better understanding of the origin of the observed LBVN morphology.

In order to investigate these questions, we have started a systematic study of a sample of LBVNs using radio and mid-IR observations. The overall idea is to obtain high-resolution images to determine the spatial variations in the components to detect particular features that can be associated with the formation and shaping mechanism. This approach has been recently used by several authors for planetary nebulae and useful information has been obtained by comparing the optical (mostly Hα) with sub-arcsec near- and mid-IR observations (Matsuura et al. 2005; Lagadec et al. 2006).

Until recently, most of the analysis of LBVN has relied on the comparison between optical (mostly Hα) and near and far-IR high-resolution images. In addition to using recombination lines

(i.e., Hα), the ionized gas in an LBVN can been traced via its free–free radio emission. Radio observations, compared to optical ones, offer the additional possibility of revealing the ionized gas well inside the dusty envelope. The radio images therefore allow us to determine in detail the spatial distribution of the ionized gas, providing useful information about the interaction between the ejecta with the surrounding medium. Finally, radio observations are a unique tool for investigating the ionized part of the circumstellar material around strongly reddened sources. In this paper, we present results on the nebula surrounding the Galactic LBV candidate HD 168625.

2. THE NEBULA ASSOCIATED WITH HD 168625

HD 168625 is a very luminous B-type star, classified between B2 and B8 (Hutsemekers et al. 1994 and references therein). The most recent distance determination for HD 168625 is 2.8 kpc (Pasquali et al. 2002). van Genderen et al. (1992) derived a bolometric magnitude of $M_{\rm BOL} = 8.6$, which places HD 168625 at the low-luminosity end of the region of the HR diagram occupied by LBVs. However, no spectroscopic variations typical of LBVs have been reported for HD 168625 in the literature in the last 50 years, hampering its classification as an LBV. Still, its physical properties and, most importantly, the characteristics of its associated nebula, which is very similar to those observed around other LBVs, strengthen the case for membership in this peculiar group of evolved massive stars. The nebula surrounding HD 168625 was first discovered by Hutsemekers et al. (1994), who noticed its complex morphology consisting of a bright central ring-like condensation and a more extended nebula, with a hint of bipolar structure. A more complete picture of the Hα nebula was obtained by Nota et al. (1996) by means of multi-epoch, high-resolution imaging and spectroscopy. The inner elliptical ring, whose major axis is oriented SE–NW, extends to $10'' \times 13''$ (or 0.14×0.18 pc, assuming a distance of 2.8 kpc), while the bipolar structure is delineated by faint filaments extending to a size of $16'' \times 24''$ (0.22×0.3 pc) and oriented perpendicularly to the inner ring. High spatial resolution Hα imaging has been obtained by Pasquali et al. (2002) with WFPC2 on the *Hubble Space Telescope* (*HST*). They find that the overall morphology is in agreement with the results of Nota et al. (1996), but the *HST* imaging reveals the much more complex filamentary structure of the shell. Pasquali et al. also measured a total dereddened Hα flux of 9.6×10^{-10} erg s^{-1} cm^{-3} and derived a total mass of ionized gas of $M_{\rm ion} \sim 2.1\, M_{\odot}$.

The inner structure of the nebula is evident in the mid-IR thermal dust emission, where the more extended bipolar structure almost disappears. The mid-IR morphologies obtained by Meixner et al. (1999) and Robberto & Herbst (1997) are both consistent with a thin, torus-shaped dusty structure, with a characteristic *horn* pattern due to geometrical projection effects. O'Hara et al. (2003) modeled the data from Meixner et al. and interpreted the dust emission from HD 168625 as a dusty torus, with a total dust mass of $(2.5 \pm 0.1) \times 10^{-3}\, M_{\odot}$. In this framework, the bipolar nebula seen in the Hα images is the result of interaction between the current fast wind of the LBV with this torus, in the form of an elliptical bubble perpendicular to the plane. Skinner (1997) reported a mid-IR spectrum showing both polycyclic aromatic hydrocarbon (PAH) and silicates features, pointing to a mixed dust composition.

Smith (2007) has reported the discovery of another component of the nebula associated with HD 168625 in the images obtained with IRAC on the *Spitzer Space Telescope*. They observe an extended ($\sim 80''$), faint outer bipolar nebula, with a well-defined polar ring. They suggest that the origin of the nebula is likely related to an LBV-like eruption from the central object. However, because of a lack of information concerning the kinematics of the system, it is not possible to assess whether the outer bipolar nebula and the inner dusty nebula are coeval.

Radio emission from HD 168625 has been detected with the ATCA (Leitherer et al. 1995). The 3.6 cm image, restored with a $3\farcs4$ beam, reveals the incomplete structure of an extended ($20'' \times 18''$) radio nebula, unbalanced with respect to the central optical position, with two bright components in the southern (peak = 1.9 mJy beam^{-1}) and in the western (peak = 1.5 mJy beam^{-1}) part of the nebula.

3. OBSERVATIONS AND DATA REDUCTION

3.1. The Mid-IR Observations

3.1.1. VISIR

To map the dust distribution in the LBVN associated with HD 168625, we have obtained high angular resolution and high sensitivity *N*- and *Q*-band images with VISIR (Lagage et al. 2004), the mid-IR imager mounted at the Cassegrain focus of the Very Large Telescope (VLT) Unit 3 telescope (MELIPAL). The observations were carried out on 2007 August 18 and 19. Images were obtained through the *PAH*2 filters, centered on known PAH features ($\lambda_c = 11.26\,\mu$m, $\Delta\lambda = 0.59\,\mu$m) and adjacent continuum (*PAH*2_2, $\lambda_c = 11.88\,\mu$m, $\Delta\lambda = 0.37\,\mu$m), and in Q1 ($\lambda_c = 17.65\,\mu$m, $\Delta\lambda = 0.83\,\mu$m). We also used the *NeII* filter ($\lambda_c = 12.80\,\mu$m, $\Delta\lambda = 0.21\,\mu$m) and its adjacent continuum (*NeII*_2$\lambda_c = 13.03\,\mu$m, $\Delta\lambda = 0.22\,\mu$m) as a tracer of ionized gas. All the observations were performed under very good and stable weather conditions, with an optical seeing better than $0\farcs6$ (August 18) and $0\farcs8$ (August 19). The target was observed at airmasses ranging between 1 and 1.4. We used a fixed pixel scale of $0\farcs127$, resulting in a field of view of $32\farcs5 \times 32\farcs5$. The standard chopping/nodding technique was adopted for subtracting the sky background as well as the telescope's thermal emission. Secondary mirror chopping was performed in the north–south direction with a chop throw of $20''$; nodding was performed in same direction as chopping, using a telescope offset of $20''$. To further improve the image quality, a random jitter pattern with a maximum throw of $3''$ was superimposed on the nodding sequence. A complete log of observations is given in Table 1. Three mid-IR standards were observed just before and after the target acquisition for flux calibration. The standard star data were also used to determine the FWHM of the observations in each band and thus to derive the angular resolution of our final maps. Values of the FWHM obtained for images in each filter are reported in the last column in Table 1.

The data were reduced following the standard VISIR pipeline (version 1.7.0), consisting of co-adding frames after flat fielding and bad pixel removal. The chopped and nodded images were than combined in a single frame per filter. The combined images are shown in Figures 5–7.

3.1.2. SPITZER/IRS

Spectral mid-IR observations were carried out using the Infrared Spectrograph (IRS; Houck et al. 2004) on board the *Spitzer Space Telescope* (Werner et al. 2004). The observations reported in this paper were part of the IRAC team GTO program (PID 30188) and were performed on 2008 May 6 (AOR 17335296). Spectra were obtained at the central source

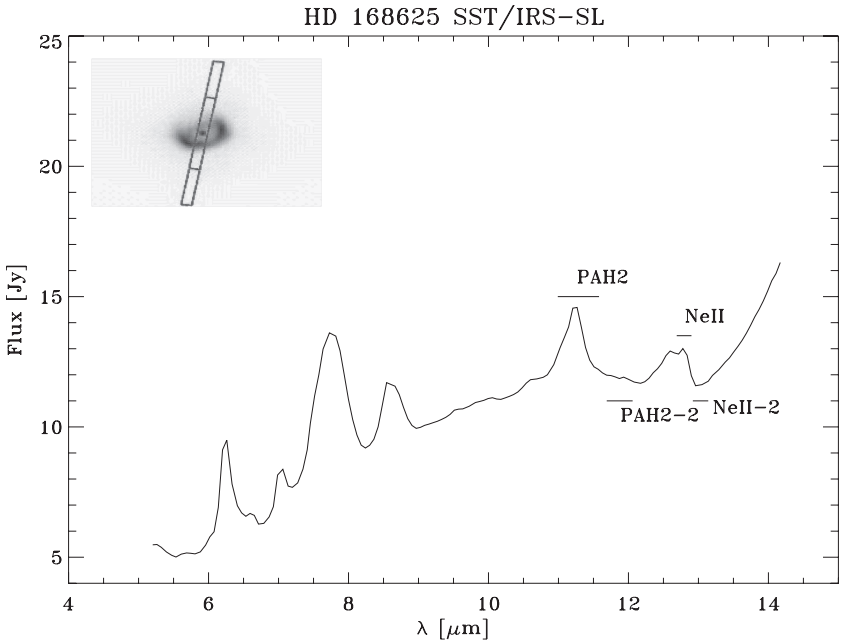

Figure 1. IRS-SL spectrum with the transmission widths of the VISIR imaging filters (*PAH*2, *PAH*2_2, *NeII*2, and *NeII*2_2) indicated. The small inset in the upper left shows the fraction of the nebula sampled by the IRS-SL module.

Table 1
VLT Observations Log

Filter	Date	UT	Integration time (*s*)	Airmass	FWHM (″)
*PAH*2	2007 Aug 18	4:35	420	1.4	0.31[a]
*PAH*2_2	2007 Aug 18	4:05	1000	1.3	0.32[a]
NeII	2007 Aug 18	3:25	1460	1.18	0.33[a]
*NeII*_2	2007 Aug 18	2:39	1800	1.08	0.34[a]
*Q*1	2007 Aug 19	2:40	1400	1.08	0.43[b]

Notes.
[a] Derived from observations of HD 216149.
[b] Derived from observations of HD 163376 and HD 198048.

position by using the IRS short–low (SL) resolution module ($64 \leqslant R \leqslant 128$, between 5.2 and 14.5 μm) in the standard staring mode on two nod positions. Three cycles were performed for each nod position in order to reject cosmic rays and other transients. Background subtraction was performed by taking advantage of the observing mode: at each nod position only one of the sub-modules, SL2 (5.2–7.7 μm) or SL1 (7.4–14.5 μm), is on the source, while the other one is observing at the sky. We therefore used these off-source observations as sky frames for the other nod position. As HD 168625 is located about 15′ southeast from the core of M17, which is surrounded by extended bright PAH emission (Povich et al. 2007), each sky frame was inspected in order to avoid any possible contamination. When pointing to the background sky, SL1 is free from contamination while SL2 has a PAH contamination of about 10% of the signal detected in the on-source position. This implies a 10% underestimate in the total intensity of the 11.2 μm PAH feature, which we take into account in the following analysis.

Background sky frames were averaged and then subtracted, before spectra extraction, by using an IDL routine written for this purpose. From the two-dimensional Basic Calibrated Data (IRS pipeline version 15.3.0), three spectra for each nod position were extracted and wavelength and flux calibration applied using the Spitzer IRS Custom Extractor (SPICE) with the extended source extraction option. The cleaning, smoothing, and merging into one final spectrum were performed by using the *Spitzer* contributed software SMART (Higdon et al. 2004). The resulting spectrum is shown in Figure 1, where the widths of the transmission curves of the VISIR image filters *PAH*2, *PAH*2_2, *NeII*2, and *NeII*2_2 are also indicated.

3.2. The Radio Observations

We observed HD 168625 with the Very Large Array (VLA) in the BnA configuration on 2006 May 26. The observations were carried out at 8.4 GHz (3.6 cm) with a total bandwidth of 100 MHz, for a total of 17 minutes of on-source integration time.

The flux density scale was determined by observing 3C286, while phase calibrations were performed with respect to the phase calibrator 1832-105. The data processing was performed using the standard programs of the NRAO Astronomical Image Processing System (AIPS) and the mapping process was performed using a natural weighting for highest sensitivity, resulting in a synthetic beam of the array ($\theta_{\rm syn}$) of $0\farcs9 \times 0\farcs6$. The final map was CLEANed and restored with a 1″ FWHM circular Gaussian beam (Figure 2). The noise level (rms) in the map was estimated by analyzing an area on the map whose distance from the phase center is greater than 100 $\theta^2_{\rm syn}$ and free from evident radio sources. The noise estimate is $\sim$0.02 mJy beam^{-1}, which is consistent with the expected theoretical noise for the integration time used.

4. THE DUSTY NEBULA

4.1. PAH Features

The mid-IR continuum-subtracted spectrum of HD 168625 is shown in Figure 3. The emission in the 5–15 μm spectral range is dominated by PAH bands, superimposed on a broad continuum, probably due to thermal emission from small grains heated to a few hundred degrees Kelvin. The C–C stretching

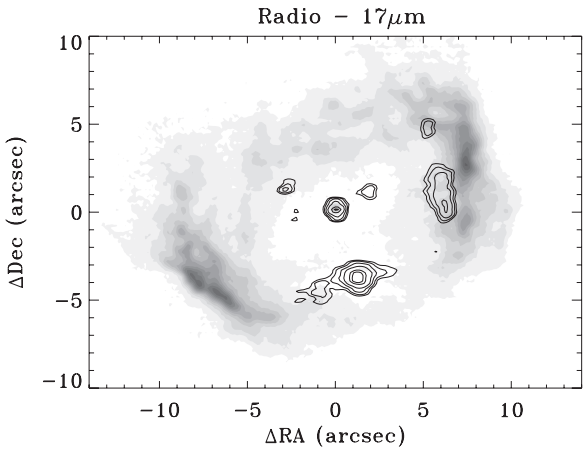

Figure 2. 3.6 cm VLA image of HD 168625 (contours) superimposed on the VLT 17 μm image (gray scale). The images are registered using the central object. The radio map has been convolved with a 1″ FWHM circular Gaussian beam. The contour levels are 0.1, 0.13, 0.17, 0.23, 0.35, 0.41, and 0.47 mJy beam^{-1}. Gray levels for the mid-IR image are 0.62, 1.24, 1.86, 2.48, 3.72, 4.34, 4.96, 5.58, 6.20 6.82, and 7.44 Jy arcsec^{-2}.

mode PAH bands at 6.2 μm and at 7.7 μm, the C–H in-plane deformation mode band at 8.6 μm, and the C–H out-of-plane deformation mode band at 11.2 μm are clearly detected. In this IRS low-resolution module, the 12.7 μm PAH band blends with the [Ne II] line at 12.8 μm. The [Ar II] 7 μm emission line is also detected, whose presence, together with that of the [Ne II] 12.8 μm, is consistent with the existence of an H II region in the nebula. Each PAH detection was identified and fit using the line-fitting routine in SMART. For each line, a local continuum was defined by a single-order fit to the baseline and the line was fit using a single Gaussian profile. The PAH band identification, central wavelength, and the derived fluxes are summarized in Table 2. For the PAH feature at 11.2 μm, the estimated background PAH contamination has been subtracted.

PAHs have been detected in many astrophysical environments (Tielens 2008). The relative strength and peak frequency of each

Table 2
PAH Bands Identifications and Observed Fluxes

Band	$\lambda(\mu m)$	$\Delta\lambda$ (FWHP)	Flux[a]
C–C 6.2	6.249	0.159	6260
C–C 7.7	7.800	0.28	12800
C–H 8.6	8.600	0.07	2890
C–H 11.2	11.25	0.09	2870[b]

Notes.
[a] Observed fluxes in units of 10^{-14} erg cm^{-2} s^{-1}. Flux uncertainties are usually $\leqslant$10%
[b] The derived flux has been corrected for the background.

of the features in the emission spectrum reflect the physical properties of the carriers and the conditions within the emission regions. A well-established characteristic of the PAH emission spectrum is its dependence on the charge of the carrier of the aromatic features (Allamandola et al. 1999). The ionization of PAH molecules results in a strong enhancement of the features in the 6–10 μm region relative to the 11.2 μm feature. This indicates that in a mixture dominated by ionized PAHs, most of the emission comes from highly vibrationally excited modes. Therefore, the ratio between the C–C and C–H feature intensities can be used as a probe of the ionization state of the PAHs, in that higher ($\frac{F_{7.7}}{F_{11.2}}$) and ($\frac{F_{6.2}}{F_{11.2}}$) ratios are indicative of a higher level of ionization. Moreover, the relative strength of different PAH bands is also indicative of PAH size; while the larger ($\frac{F_{7.7}}{F_{11.2}}$) ratio is consistent with ionized PAHs, for both neutral and ions the ($\frac{F_{6.2}}{F_{7.7}}$) ratio tends to decrease as the number of carbon ions in the molecule is increasing (Draine & Li 2001).

The low-resolution IRS modules have a long slit (57″) with a width of 3.″7. This means that only part of the nebula was sampled in our observation (see the small inset in Figure 1). Therefore, if we want to use the relative strength of different PAH bands to derive physical characteristics of the PAH component, we need to assume that the physical properties of PAHs are similar over the entire nebula. The ratios of the

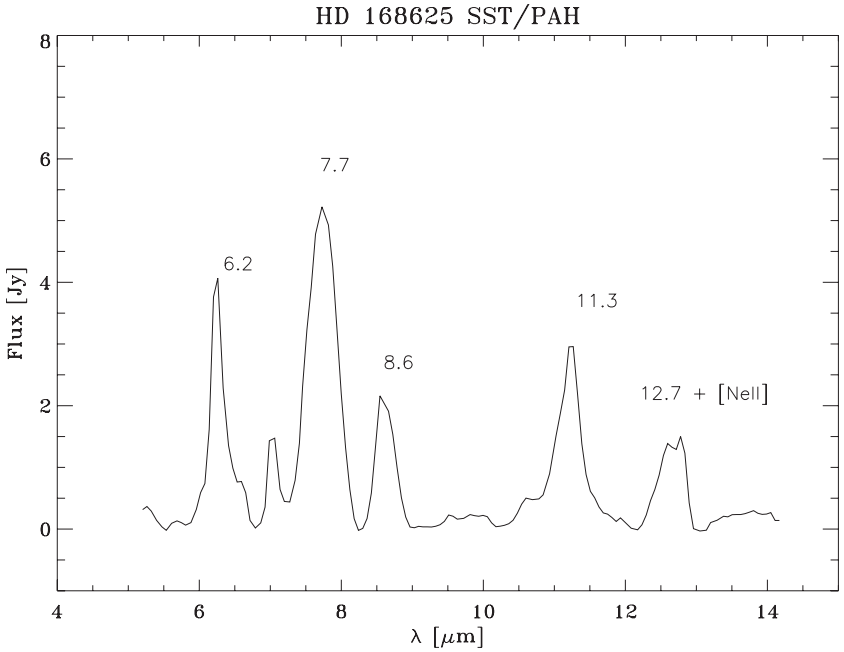

Figure 3. Continuum-subtracted spectrum of HD 168625 with the PAH bands identified. The PAH band at 12.7 μm blends with the [Ne II] line at 12.8 μm.

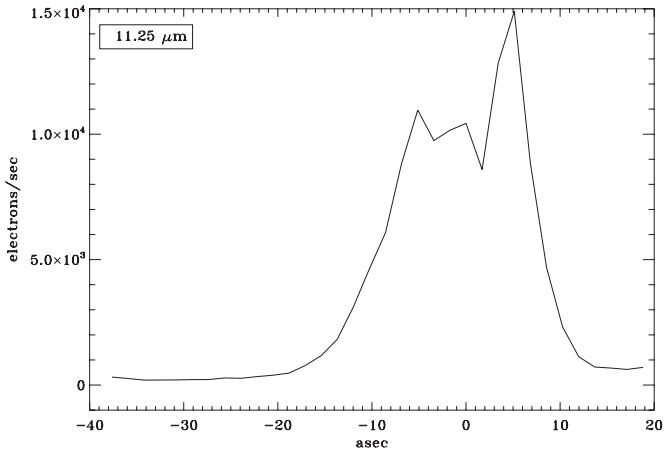

Figure 4. Brightness along the slit for the 11.3 μm PAH feature. The brightness is measured from the central position with increasing values (positive) going in the SE direction.

PAH features are $\frac{F_{7.7}}{F_{11.2}} = 4.5$, $\frac{F_{6.2}}{F_{11.2}} = 2.2$, and $\frac{F_{6.2}}{F_{7.7}} = 0.49$ (see Table 2) and we conclude that the PAHs detected in the dusty nebula of HD 168625 are mostly ionized, as consequence of the strength of the radiation field which they are exposed to (Galliano et al. 2008). These ratios also indicate that the PAHs consist on average of a small number (20–60) of carbon ions (Draine & Li 2001).

Peeters et al. (2002) have classified different types of objects on the basis of their PAH emission spectrum. In this scenario, HD 168625 falls in their B class, characterized by a shift of the peak of the 6.2 μm and at 7.7 μm features to longer wavelengths. Typically, the B class consists of evolved objects with associated circumstellar envelopes.

We can also derive some information on the spatial distribution of the PAHs from our IRS spectra. To do this, we inspect the two-dimensional spectra before extraction and perform a cut along the 57″ NW–SE oriented IRS slit (see Figure 1) for each PAH feature. As an example, in Figure 4, we show the brightness (in electrons per second) of the 11.3 μm PAH feature as function of position (in arcseconds) from the central object. A strong asymmetry is evident in the PAH feature, with stronger emission coming from the SE region. The plot shows a sharp drop in the brightness distribution in the SE region and a more slowly declining shoulder in the NW region. Such behavior is common to all of the PAH features and may indicate that the PAH emission is more diffuse up to 15″ from the central object in the NW part of the nebula.

In principle, the extended, faint outer bipolar nebula reported by Smith (2007) may also contribute to the observed PAH emission, as that location is sampled by the IRS slit. The fact that the extended component is visible at 4.5 μm and 8.0 μm but not in the 5.8 μm IRAC band already indicates that the origin of the emission is not related only to strong PAH components but probably to a combination of different processes, such as atomic line emission, scattered starlight, and warm dust emission as well as PAHs. However, no contribution from the extended component or diffuse emission from other part of the lobes is evident from 15″ up to 40″ from the central object and, if it exists, must be on the order of a few (two to three) percent or less.

4.2. The Nebula Morphology

The morphology of the dusty nebula is evident in our mid-IR images. All of the VISIR images (Figures 5–7) reveal a

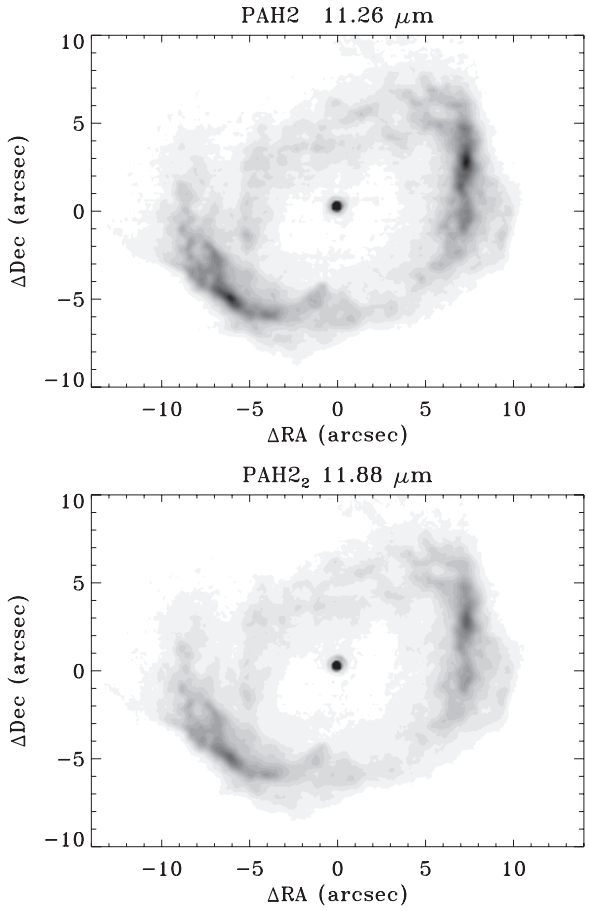

Figure 5. VISIR maps of HD 168625 on the 11.2 μm PAH feature (upper panel) and the adjacent continuum (lower panel). In both panels, the brightness levels range from 0 to 2.48 Jy arcsec^{-2}. The central star has a peak of 10.95 and 10.58 Jy arcsec^{-2} in the two maps. The brightest point in the nebula is 2.41 Jy arcsec^{-2} and 1.82 Jy arcsec^{-2}, respectively.

torus-like structure whose overall shape was already reported by Meixner et al. (1999) and Robberto & Herbst (1997). However, the higher resolution and sensitivity of our images allow us to discern finer details of the dust distribution, most notably the highly structured texture of the nebula, and provide a better localization of the dust ring, with its northwest and southeast condensations. A more extended emission is also evident, which is probably associated with the bipolar nebula and perpendicular to the equatorial dust ring, as foreseen by the scenario proposed by O'Hara et al. (2003). All of the arch-like structures reported by Robberto & Herbst (1997) and the southern cusp-like feature, which is among the brightest features in the near-IR (NICMOS O'Hara et al. 2003) and mid-IR images, are well defined in our VISIR images. The structure reported as prominent in the V-continuum map and identified as "arm" (Pasquali et al. 2002) is also well detected in all of the VISIR images. There is a general trend in the dust emission to be more prominent in the southern part of the shell for $\lambda \leqslant 13\,\mu$m, while in the Q-band image most of the dust emission originates in the northern part of the nebula. Indeed, at increasing wavelengths, the cusp feature, which is very bright at 11.26 μm, is less defined, merging with the underlying faint diffuse emission at 17.65 μm. This spatial dependence of the dust emission at different wavelengths has also been reported by O'Hara et al. (2003), who interpreted it in terms of variations in the grain size in different regions of the nebula, or to a gradient in the dust/gas ratio.

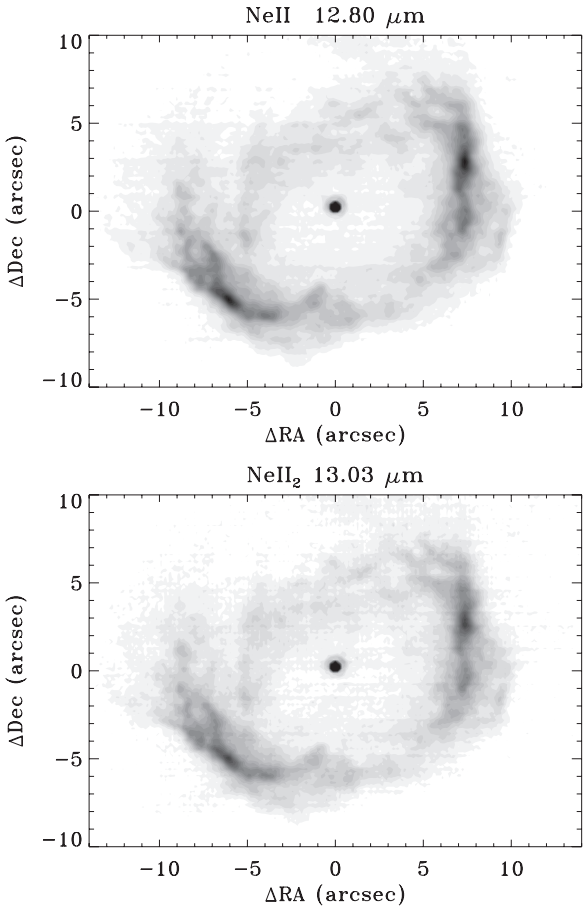

Figure 6. VISIR maps of HD 168625 in the [Ne II] line (upper panel) and adjacent continuum (lower panel). In both panels, the brightness levels range from 0 to 1.86 Jy arcsec^{-2}. The central star has a peak of 9.0 and 9.22 Jy arcsec^{-2} in the two maps. The brightest point in the nebula is 1.82 Jy arcsec^{-2} and 1.61 Jy arcsec^{-2}, respectively.

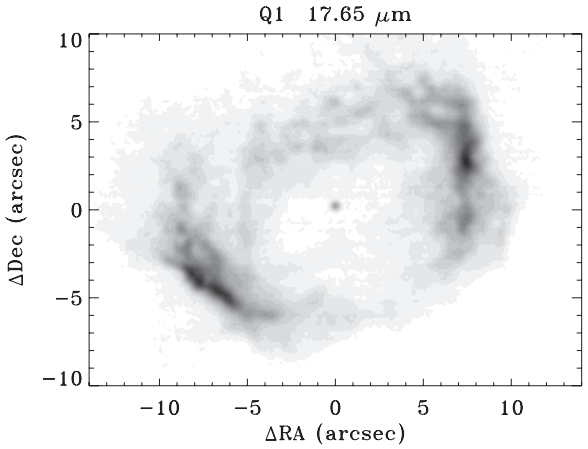

Figure 7. VISIR map of HD 168625 in the Q1 continuum filter. The brightness levels range from 0 to 8.06 Jy arcsec^{-2}. The central star has a peak of 3.62 Jy arcsec^{-2}, and the brightest point in the nebula is 7.58 Jy arcsec^{-2}.

The nebula is well detached from the central object, which is clearly detected from 11.26 μm to 17.65 μm. We performed aperture photometry of the central object in each image by using the IDL procedure ATV, while the nebula contribution at each wavelength was determined by integrating the flux emitted in a $12'' \times 12''$ area. The photometry results are summarized in Table 3, and are in good agreement with the spectral energy distribution reported by Robberto & Herbst (1997).

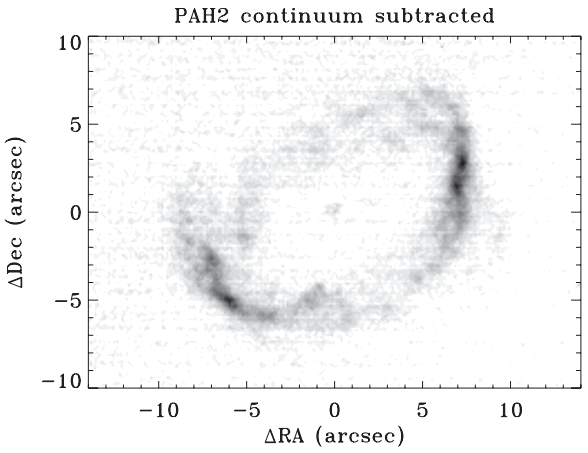

Figure 8. Map of the PAH2 (11.26 μm) emission, after subtraction of the adjacent continuum image. The brightest point in the nebula is 0.62 Jy arcsec^{-2}.

Table 3
Mid-IR Photometry

Filter	$F_{\rm Star}$ (Jy)	$F_{\rm Nebula}$ (Jy)
PAH2	1.77	103
PAH2_2	1.61	87
NeII	1.54	91
NeII_2	1.52	83
Q1	0.61	429

We examined the spatial distribution of the PAH feature at 11.26 μm by subtracting the image obtained at the adjacent continuum (*PAH2_2*) from the PAH2 image, after co-aligning the images relative to the central object. The 11.26 μm PAH feature emission in Figure 8 appears to be concentrated in a thin disk, the same region where most of the thermal dust continuum emission originates, with a slightly higher concentration on the southern part of the ring where the cusp feature is well delineated. There is no evidence of a PAH contribution to the more diffuse nebula. The morphology of our *Q*-band image (Figure 7) is highly structured in the northern part of the nebula, with strong similarities to the *Paddle* structure observed in the V-continuum image by Pasquali et al. (2002). As the V image traces the light scattered by dust, this result is consistent with a population of large grains (having a higher scattering efficiency) being more localized in the northern part of the nebula.

These images provide observational evidence that the dust distribution in the LBVN is not homogeneous, and different populations of dust grains and PAHs coexist. In general, thermal dust grains of different sizes responsible for the continuum have the same spatial distribution, but there are some regions dominated by PAHs and smaller grains and other regions with a more prominent contribution from larger grains. This may also reflect a different dust composition in the nebula where carbonaceous dust as well as silicates appear to coexist (Skinner 1997).

In principle, we could also determine the spatial distribution of the [Ne II] emission (which should trace the ionized gas) following the same procedure, i.e., by subtracting the adjacent continuum image at 13.03 μm (*NeII_2*) from the 12.80 μm image. However, as evident from Figure 1, the *NeII* VISIR filter that should sample the [Ne II] emission is strongly contaminated by the 12.7 μm PAH emission and the resulting image does not provide a reliable ionized gas tracer. Unfortunately, we did not

have detailed information on the mid-IR spectrum of HD 168625 available prior to our VISIR observations.

4.3. Temperature and Optical Depth Maps

In order to better understand the physical properties of emitting grains, we constructed temperature and optical depth maps from the our mid-IR images following Dayal et al. (1998). This method assumes that the emission is purely thermal and the dust in the shell is at thermal equilibrium. Therefore, in the following analysis, to avoid PAH emission which arises from transiently heated grains, we have used the *PAH2_2* (*PAH2* adjacent continuum) plus the *Q* images. The same results would have been achieved if the *NeII* adjacent continuum, instead of *PAH2_2*, was used, as the two continuum images are almost identical. Both the *PAH2_2* and *Q* images were smoothed to the same spatial resolution and co-aligned using the central object.

The dust temperature T was calculated assuming that the circumstellar envelope is optically thin. In this case, the observed intensity is given by

$$I_\nu \approx B_\nu(T)\tau_\nu. \quad (1)$$

Using the Wien approximation ($h\nu \gg kT$) for the blackbody expression $B_\nu(T)$, the ratio of the intensities at two different frequencies ν_1 and ν_2 is given by

$$\frac{I_{\nu_1}}{I_{\nu_2}} = e^{-h(\nu_1-\nu_2)/kT}\left(\frac{\lambda_2}{\lambda_1}\right)^3 \frac{\tau_{\lambda_1}}{\tau_{\lambda_2}}. \quad (2)$$

The optical depth τ_λ is proportional to the absorption cross section of the dust grains, which in turn depends on its chemical composition and the grain size a. However, for $\lambda > 1\,\mu$m and for a grain size $a < 0.1\,\mu$m, it is almost constant (van Hoof et al. 2004). We compute the absorption coefficient as a function of the wavelength for astronomical silicate and graphite for grain sizes of $a = 0.01,\ 0.1$, and $1\,\mu$m using the code CLOUDY (Ferland et al. 1998). For our images at $\lambda_1 = 11.88$ and $\lambda_2 = 17.65\,\mu$m, we found $\tau_{\lambda_1}/\tau_{\lambda_2} = 1.05$ in the case of graphite and 1.27 in the case of astronomical silicates.

For each pixel of the map, we derived the dust temperature by inverting Equation (2):

$$T \approx 1.44 \times 10^4 \frac{\left(\lambda_2^{-1} - \lambda_1^{-1}\right)}{\ln\left[\frac{I_{\nu_1}}{I_{\nu_2}}\frac{\tau_{\lambda_2}}{\tau_{\lambda_1}}\left(\frac{\lambda_1}{\lambda_2}\right)^3\right]}. \quad (3)$$

The dust temperature was computed only at those pixels whose surface brightness is greater than 0.06 Jy arcsec^{-2}, corresponding to 3σ in the maps. In this derivation, we assumed a constant temperature along the line of sight for each pixel. The resulting dust temperature map is shown in Figure 9. For the case of graphite grains, the dust temperature ranges from 110 to 210 K, reaching the highest value in the southern part of the shell. Slightly lower temperature values (∼10%) are obtained if a mixture of silicate grains is assumed instead.

The optical depth map at $\lambda = 17.65\,\mu$m was calculated by inverting Equation (1), using the value of the temperature and observed intensity at each point in the map. The optical depth map obtained assuming graphite is shown in Figure 9. The maxima in the optical depth image are found in the eastern ($\tau = 0.023$) and western ($\tau = 0.012$) parts of the nebula, while the minima are in the northern (0.003) and southern (0.0004) regions. In the case of silicates, the optical depth is about 50% higher.

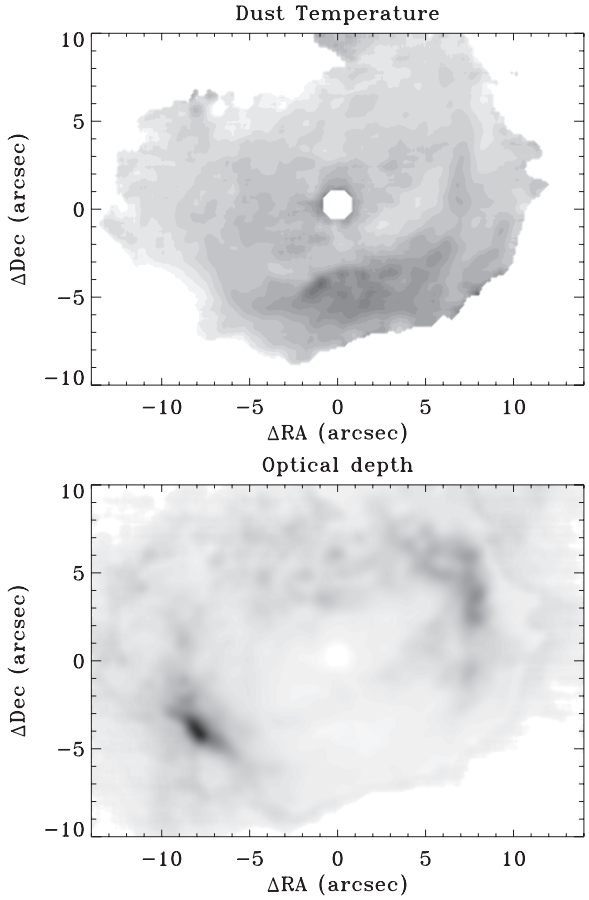

Figure 9. Upper panel: temperature map for the case of graphite; the temperature ranges from 110 to 210 K. Lower panel: optical depth map for the case of graphite; the maximum value is $\tau = 0.023$.

4.4. The Mass of the Dust

The mass of the dust envelope can be evaluated from the optical depth map and the absorption coefficient per mass unit $k_{\rm dust}$. If the medium is homogeneous, the optical depth is given by $\tau = k_{\rm dust}\,\rho_{\rm dust}\,l$, where $\rho_{\rm dust}$ and l are the density of the medium and the thickness of the envelope. We computed the absorption coefficient by using CLOUDY in the case of graphite (carbon abundance: $n({\rm C})/n({\rm H}) = 2.78 \times 10^{-4}$) and astronomical silicates ($MgSiFeO_4$, $n({\rm Mg})/n({\rm H}) = n({\rm Si})/n({\rm H}) = n({\rm Fe})/n({\rm H}) = 3.28 \times 10^{-5}$ and $n({\rm O})/n({\rm H}) = 1.31 \times 10^{-4}$). Since CLOUDY gives the absorption cross section per unit hydrogen nucleon for a given abundance of the constituents of the grain molecule (σ, in cm^2 H^{-1}), we compute the absorption coefficient for mass unit as

$$k_{\rm dust} = \sigma \times \frac{N_{\rm x}}{n({\rm x})/n({\rm H})}\frac{1}{m_{\rm D}}, \quad (4)$$

where $N_{\rm x}$ is the number of atoms constituting a given dust grain, $n({\rm x})/n({\rm H})$ is the total abundance of those atoms with respect to the total hydrogen nucleons, and $m_{\rm D}$ is the mass of a single dust grain. The mass absorption coefficients for graphite and silicate computed for three grain sizes are shown in Figure 10. The values obtained for $k_{\rm dust}$ at $\lambda = 60\,\mu$m are about 145 and 94 cm^2 g^{-1} for graphite and silicates, respectively, and are in good agreement with Stasińska & Szczerba (1999). At $\lambda = 17\,\mu$m, we found $k_{\rm dust} = 253$ and 1082 cm^2 g^{-1} for graphite and silicates, respectively. The mass behind each map pixel, whose size is 0.″127, is given by $\Delta m = \tau/k \times \Delta A$,

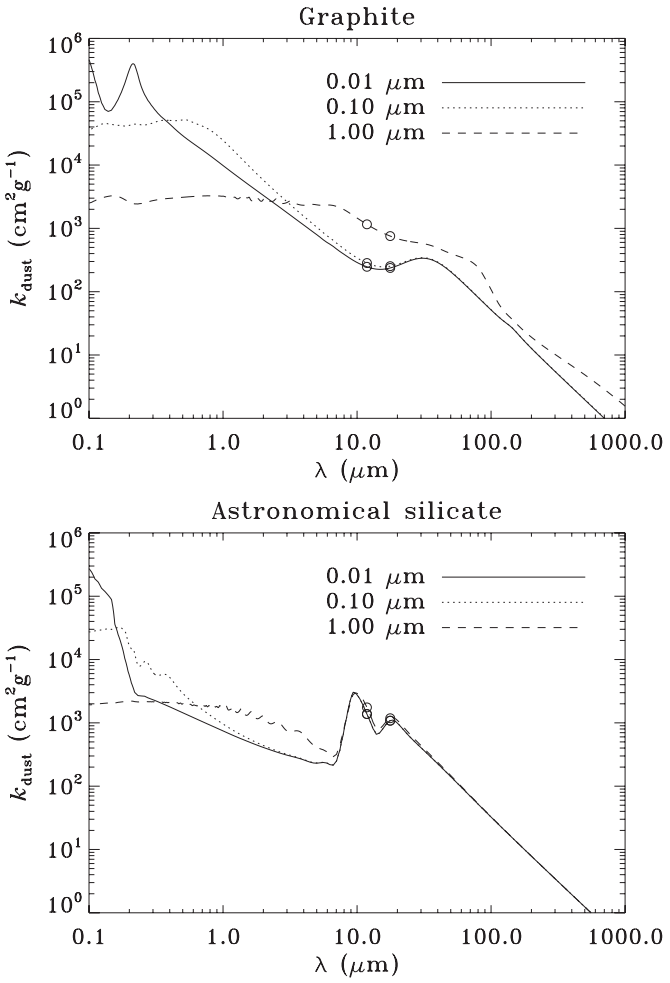

Figure 10. Absorption coefficients per mass unit for graphite (upper panel) and astronomical silicates (bottom panel), for different values of the dust grain size.

where ΔA is the area source corresponding to one map pixel, or 2.8×10^{31} cm^2 assuming a distance of 2.8 kpc (Pasquali et al. 2002).

Integrating over all the pixels with brightness higher than 3σ, we derive a total dust mass of 1.9×10^{31} g ($10^{-3}\ M_\odot$) in the case of graphite, and 2.9×10^{31} g ($1.4 \times 10^{-3}\ M_\odot$) in the case of silicates. This should be considered a lower limit for the total mass of the nebula, as the emission at 17.0 μm traces only the warm dust. We expect a cold dust component as well as an important ionized gas component to coexist in the nebula.

5. THE IONIZED NEBULA

The radio emission traces the ionized part of the nebula without suffering from the intrinsic extinction due to the presence of dust. The observations reported in this paper were designed to map the inner part of the radio nebula in order to detect the stellar wind from the central object. Therefore, the higher angular resolution, compared to that achieved with ATCA, allows us to resolve the nebula into several compact components. However, this prevents a good sampling of the more extended radio emission. Our result confirms the presence of an incomplete radio nebula (Leitherer et al. 1995) which is characterized by a clumpy morphology with several bright components (Figure 2). The southern and the western compact components pointed out earlier by Leitherer et al. (1995) are clearly distinguished, as well as a central unresolved component,

Table 4
Radio Properties of the Bright Components

	JMFIT		TVSTAT	
Component	Flux Density (mJy)	α_{2000}	δ_{2000}	Flux Density (mJy)
S	1.04 ± 0.02	182119.46	−162229.9	1.47 ± 0.02
Central	0.42 ± 0.02	182119.5	−162226.0	
W	1.16 ± 0.02	182119.13	−162225.16	1.42 ± 0.02

whose coordinates coincide with the optical position of the star and is probably related to the stellar wind of the LBV. The position and the flux density of these components have been derived by fitting a two-dimensional Gaussian brightness distribution to the map (AIPS task JMFIT), and are summarized in Table 4.

We partially recover the flux densities for the southern and western components reported by Leitherer et al. (1995) if, instead of fitting with a Gaussian, we sum the contribution of all the pixels in the region occupied by the single radio component (AIPS task TVSTAT). This indicates that around the western and southern compact components, there is extended radio flux in the nebula that the present observations resolve out. Another indication of extended radio emission which is missed in our map comes from the fact that we observed a total flux of 5.2 ± 0.1 mJy, as derived by integrating over all the pixels within the radio nebula, while Leitherer et al. (1995) measured a total of 14 ± 2 mJy at the same frequency.

We can derive the current day LBV mass-loss rate from the radio flux density of the central unresolved radio source, assuming that emission is due to the stellar wind. Panagia & Felli (1975) derived standard formulae for thermal radio emission from an expanding wind, relating the observed radio flux (F_ν) to the dynamical parameters of the wind such as mass-loss rate ($\dot{M}$) and the terminal velocity of the wind (v_∞). We can therefore estimate the mass-loss rate by using the relation:

$$\dot{M} = 0.32 \times 10^{-5} v_\infty F_\nu^{3/4} D_{\rm kpc}^{3/2}\ M_\odot\ {\rm yr}^{-1}, \qquad (5)$$

where full ionization, cosmic abundances, and a wind temperature of 10^4 K have been assumed. F_ν is expressed in mJy and v_∞ in 10^3 km s^{-1}.

From the measured radio flux density at 8.4 GHz, assuming a current LBV outflow of $v = 183$ km s^{-1} (Nota et al. 1996) and the revised distance of 2.8 kpc (Pasquali et al. 2002), we derive a mass-loss rate of $\dot{M} = (1.46 \pm 0.15) \times 10^{-6}\ M_\odot\ {\rm yr}^{-1}$. This result is consistent with the value of $\dot{M} = 1.1 \times 10^{-6}\ M_\odot\ {\rm yr}^{-1}$ obtained by Nota et al. (1996) from their analysis of the Hα profile, which assumed a distance of 2.2 kpc to HD 168625.

High angular resolution *HST* observations of the nebula surrounding HD 168625, which could in principle trace the ionized gas component, have been obtained in Hα (Pasquali et al. 2002) and at 2.2 μm (O'Hara et al. 2003). The 2.2 μm NICMOS image reveals an unbalanced nebula with a fragmented southern bright rim. However, this image, obtained with a bandwidth of $\sim$0.15 μm, is a combination of both warmer dust and recombination line (Bracket γ at 2.166 μm) emission, and cannot be used as a pure ionized gas tracer. More interesting for our purposes is the *HST* Hα image. Most of the Hα emission arises from an elliptical shell whose orientation and dimensions are very close to that of the dust emitting region. A very faint loop is barely visible in the northern region. While a comparison of the diffuse radio and Hα emission does not reveal any substantial

differences (Leitherer et al. 1995), some are visible in the high-resolution images. The brighter Hα emission is localized in the southern part of the nebula, and in particular, the southern brightest compact structure is at 3″ from the central object and is coincident with the southern compact radio source detected at 3.6 cm. No obvious compact Hα counterpart of the western radio component is visible, only diffuse emission is seen. This could indicate a strong intrinsic extinction in the western part of the nebula and a much reduced dust optical thickness in the southern regions.

6. CONCLUSIONS

We have performed mid-IR observations, both imaging and spectroscopic, and radio imaging observations of the Galactic LBV candidate HD 168625 and its associated nebula. The mid-IR spectrum, obtained as a part of a *Spitzer*/IRAC team GTO program aimed at studying stellar ejecta from evolved stars, has revealed the presence of spectral features attributed to PAHs. Emission from the C–H out-of-plane deformation mode at 11.2 μm was first detected in this object by Skinner (1997), but the higher quality of our *Spitzer* IRS-SL spectrum allows us to confirm the 11.2 μm detection, to detect other PAH bands, and to estimate the flux in each PAH band. With the caveat that the SL slit only sampled part of the nebula, from the analysis of the mid-IR spectrum some physical properties of the PAHs have been derived. The PAHs appear to be ionized and, on average, to consist of a small number of carbon ions.

The detection of spectral features due to PAHs in the circumstellar material associated with an evolved star is very important. First, the PAH features are excited by soft ($\lambda \geqslant 912$ Å) UV photons that can pass through the hydrogen ionization front, and therefore they are an indication of a photodissociation region (PDR) surrounding the ionized part of the LBVN. The gas is predominantly neutral but its chemistry and thermal balance are controlled by FUV photons. There is growing evidence for the presence of PDRs around LBVs via the detection of low-excitation atomic fine structure line (Umana et al. 2009) or molecular (CO) emission (Nota et al. 2002; Rizzo et al. 2008).

A possible key role for LBVs in the scenario of massive star evolution has been proposed by Lamers et al. (2001). However, to reproduce correctly the transition between O and W-R stars, evolutionary models need a crucial piece of information that is currently incomplete, i.e., the total amount of mass lost during the LBV phase. In this context, it is therefore very important to characterize the neutral/molecular gas component surrounding these hot stars that, in addition to the ionized and dust components, must be included to determine the total mass lost from the star.

Second, as they evolve and experience massive mass loss, LBVs expose layers of CNO-cycle processed material with C and O gas phase abundances strongly depleted in favor of N gas phase abundance. Dust forms in such ejecta and we expect the dust mixture, which critically depends on the gas phase abundances, to be quite different from asymptotic giant branch (AGB) dust (Gail et al. 2005). Indeed, examples of O-rich dust (both amorphous and crystalline) have been reported in the literature (Waters et al. 1998; Umana et al. 2009), with HD 168625 an example of possible mixed chemistry (this paper). The presence of carbon-based molecules in a massive evolved star such as HD 168625 could be extremely relevant to the studies of transient sources like SN2008S and NGC 300-OT, whose nature is still uncertain. Mid-IR observations have recently provided important clues about the progenitor, which, in both cases, is consistent with a low-luminosity dust-enshrouded star (Prieto et al. 2008, 2009). In addition to other possible scenarios, the origin of the transients has been associated with a process similar to an LBV burst (Smith et al. 2009) or to something uniquely occurring in extreme AGB stars with lower masses (Thompson et al. 2009; Botticella et al. 2009). Prieto et al. (2009) pointed out that the presence of PAH-like features in the spectrum of NGC 300-OT indicates a carbon-rich environment. This points to a low-mass, carbon-rich progenitor, since more massive stars are expected to form only O-based dust and show silicates features. The detection of C-based molecules in a massive star like HD 168625 opens new possibilities for the origin of such transients and weakens the low-mass progenitor hypothesis. This is further corroborated by the recent discovery of an LBV progenitor for two optical transients (Smith et al. 2010), strongly suggesting that such events are related to an LBV-type outburst.

Our new VISIR maps confirm the overall mid-IR morphology of the dusty nebula as previously reported. However, the higher spatial resolution, sensitivity, and dynamic range of our observations have provided images with much finer details than in earlier studies. In particular, there is evidence for morphological changes in the nebula as a function of wavelength which are related to grain population differences (smaller grains more concentrated in the southern regions versus larger grains concentrated in the northern regions of the nebula). This has also been confirmed by the $\lambda = 17.65\,\mu$m optical depth map, which shows a stronger contribution from larger grains in the northern part of the nebula.

The PAH2 and adjacent continuum images have been used to isolate and spatially localize the 11.2 μm emission. PAHs appear to be more localized where most of the thermal dust emission originates, with no or very little contribution from the more extended nebula. Moreover, the PAH distribution is slightly enhanced in the southern part of the nebula.

We have used high angular resolution radio (3.6 cm) observations to trace the ionized component of the stellar ejecta via its free–free emission. The aim of the radio observations was to resolve the stellar wind from the central object. While the main goal has been achieved allowing us to estimate the current mass-loss rate from the central star, we were not able to recover fully all the extended nebula emission. We can, however, confirm the presence of an asymmetric radio nebula as previously reported by Leitherer et al. (1995). It is interesting that several asymmetric ionized nebulae have now been reported around known Galactic LBVs. For example, an extremely imbalanced radio nebula morphology has been observed in IRAS 18576+0341 (Umana et al. 2005), HR Car (White 2000), and in the Pistol star (Lang et al. 1999). Only in the case of the Pistol star can the nebula be traced to external sources of ionizing flux, which is probably related to the numerous OB stars in the Quintuplet cluster (Lang et al. 1999). For HR Car and IRAS 18576+0341, even though many possible causes for the origin of their observed radio morphology have been proposed, no firm conclusions have been reached.

The new mid-IR images closely match the radio map, allowing a detailed comparison between mid-IR and radio morphologies which in principle could help in discriminating between possible shaping processes. When, after convolving to the same spatial resolution, we superimpose our VLA-A snapshot on the *Q*-band VLT image (Figure 2), some differences between the ionized gas and dust distributions are evident. In particular, the bright southern radio component corresponds to

a hole in the dust emission, confirming the scenario developed from the previous Hα/radio comparison. The dust emission hole may be interpreted as a lack of thermal grains in that region evocative of grain–grain collisions (shattering) of big grains due to a strong, asymmetric mass loss traced by the radio. Passing shock waves can shatter grains and efficiently change the grain size distribution by fragmenting bigger grains into smaller ones with a range of sizes (Tielens 2008). Jones et al. (1996) have considered the effect of shattering in typical interstellar shocks ($v_S \sim 100\,\mathrm{km\,s^{-1}}$), which may transform carbon dust into small carbon clusters; in such cases PAHs and very small grains may be considered to be the fragmented products of the shattering process. In this scenario, the southern component may be considered as a fingerprint of a shock due to the interaction of a fast outflow ($v \sim 180\,\mathrm{km\,s^{-1}}$; Nota et al. 1996) with the slower dusty shell ($v \sim 20-30\,\mathrm{km\,s^{-1}}$; Pasquali et al. 2002). The presence of PAHs and small grains that are more concentrated in the southern region, where the shock manifests itself, fits into this picture very well. This result constitutes a piece of observational evidence in favor of an asymmetric mass loss from the central object excavating a breach in the molecular/dusty envelope.

We thank an anonymous referee for the extremely helpful suggestions that improved the paper. We acknowledge partial financial support from the ASI contract I/016/07/0 "COFIS" and from PRIN-INAF 2007. This work is based in part on observations made with the *Spitzer Space Telescope*, which is operated by the Jet Propulsion Laboratory, California Institute of Technology under NASA contract 1407. Support for this work was provided by NASA through contract number 1256790 issued by JPL/Caltech. The IRS was a collaborative venture between Cornell University and Ball Aerospace Corporation funded by NASA through the Jet Propulsion Laboratory and Ames Research Center. This work is based also on observations made with the VISIR instrument on the ESO VLT telescope (program ID. 079.D-0748A). The Very Large Array is a facility of the National Radio Astronomy Observatory, which is operated by Associated Universities, Inc., under cooperative agreement with the National Science Foundation. SMART was developed at Cornell University and is available through the Spitzer Science Center at Caltech.

Facilities: Spitzer (IRS), VLT:Melipal (VISIR), VLA.

REFERENCES

Allamandola, L. J., Hudgins, D. M., & Sandford, S. A. 1999, ApJ, 511, L115
Botticella, M. T., et al. 2009, MNRAS, 398, 1041
Clark, J. S., Egan, M. P., Crowther, P. A., Mizuno, D. R., Larionov, V. M., & Arkharov, A. 2003, A&A, 412, 185
Clark, J. S., Larionov, V. M., & Arkharov, A. 2005, A&A, 435, 239
Davies, B., Oudmaijer, R. D., & Vink, J. S. 2005, A&A, 439, 1107
Dayal, A., Hoffmann, W. F., Bieging, J. H., Hora, J. L., Deutsch, L. K., & Fazio, G. G. 1998, ApJ, 492, 603
Draine, B. T., & Li, A. 2001, ApJ, 551, 807
Ferland, G. J., Korista, K., Vernet, D., Ferguson, J., Kingdon, J., & Verner, E. 1998, PASP, 110, 761
Frank, A., Ryu, D., & Davidson, K. 1998, ApJ, 500, 291
Gail, H. P., Duschl, W. J., Ferrarotti, A. S., & Weis, K. 2005, in ASP Conf. Ser. 332, The Fate of the Most Massive Stars, ed. R. M. Humphrey & K. Z. Stanek (San Francisco, CA: ASP), 317
Galliano, F., Madden, S. C., Tielens, A. G. G. M., Peeters, E., & Jones, A. P. 2008, ApJ, 679, 310
Hidgon, S. J. U., et al. 2004, PASP, 116, 824
Houck, J., et al. 2004, ApJS, 154, 18
Hutsemekers, D., Van Drom, E., Gosset, E., & Melnick, J. 1994, A&A, 290, 906
Jones, A. P., Tielens, A. G. G. M., & Hollenbach, D. J. 1996, ApJ, 469, 740
Lagadec, E., et al. 2006, A&A, 448, 203
Lagage, P. O., et al. 2004, Messenger, 117, 12
Lamers, H. J. G. L. M., Nota, A., Panagia, N., Smith, L. J., & Langer, N. 2001, ApJ, 551, 754
Lang, C. C., Finger, D. F., Goss, W. M., & Morris, M. 1999, AJ, 118, 2327
Leitherer, C., Chapman, J. M., & Koribasky, B. 1995, ApJ, 450, 289
Maeder, A., Meynet, G., & Hirschi, 2005, in ASP Conf. Ser. 332, The Fate of the Most Massive Stars, ed. R. M. Humphrey & K. Z. Stanek (San Francisco, CA: ASP), 3
Matsuura, M., Zijlstra, A. A., Molster, F. J., Waters, L. B. F. M., Nomura, H., Sahai, R., & Hoare, M. G. 2005, MNRAS, 359, 383
Meixner, M., et al. 1999, ApJS, 122, 221
Nota, A., Pasquali, A., Clampin, M., Polacco, D., Scuderi, S., & Livio, M. 1996, ApJ, 473, 946
Nota, A., Pasquali, A., Marston, A. P., Lamers, H. J. G. L. M., Clampin, M., & Schulte-Ladbeck, R. E. 2002, AJ, 124, 2920
Nota, A., Livio, M., Clampin, M., & Schulte-Ladbeck, R. 1995, ApJ, 448, 788
O'Hara, T. B., Meixner, M., Speck, A. K., Ueta, T., & Bobrowsky, M. 2003, ApJ, 598, 1255
Panagia, N., & Felli, M. 1975, A&A, 39, 1
Pasquali, A., Nota, A., Smith, L. J., Akiyama, S., Messineo, M., & Clampin, M. 2002, ApJ, 124, 1625
Peeters, E., et al. 2002, A&A, 390, 1089
Prieto, J. L., Sellgren, K., Thompson, T. A., & Kochanek, C. K. 2009, ApJ, 705, 1425
Prieto, J. L., et al. 2008, ApJ, 681, L9
Povich, M. S., et al. 2007, ApJ, 660, 346
Rizzo, J. R., Jimenez-Esteban, F. M., & Ortiz, E. 2008, ApJ, 681, 355
Robberto, M., & Herbst, T. M. 1997, ApJ, 498, 400
Skinner, C. J. 1997, PASP, 120, 322
Smith, N. 2007, AJ, 133, 1034
Smith, N., & Owocki, S. P. 2006, ApJ, 645, L45
Smith, N., et al. 2009, ApJ, 697, L49
Smith, N., et al. 2010, AJ, 139, 1451
Stasińska, G., & Szczerba, R. 1999, A&A, 352, 297
Tielens, A. G. G. M. 2008, ARA&A, 46, 289
Thompson, T. A., Prieto, J. L., Stanek, K. Z., Kistler, M. D., Beacom, J. F., & Kochanek, C. S. 2009, ApJ, 705, 1364
Umana, G., Buemi, C. S., Trigilio, C., Hora, J. L., Fazio, G. G., & Leto, P. 2009, ApJ, 694, 697
Umana, G., Buemi, C. S., Trigilio, C., & Leto, P. 2005, A&A, 437, L1
van Genderen, A. M. 2001, A&A, 366, 508
van Genderen, A. M., et al. 1992, A&A, 264, 88
van Hoof, P. A. M., Weingartner, J. C., Martin, P. G., Volk, K., & Ferland, G. J. 2004, MNRAS, 350, 1330
Waters, L. B. F. M., Morris, P. W., Voors, R. H. M., Lamers, H. J. G. L. M., & Trams, N. R. 1998, Ap&SS, 255, 179
Weis, K. 2008, in Clumping in Hot-Star Winds: Proceedings of an International Workshop held in Potsdam, Germany, 2007 June 18–22, ed. W. R. Hamann, A. Feldmeier, & L. M. Oskinova (Potsdam: Univ.-Verl), 183
Werner, M., et al. 2004, ApJS, 154, 1
White, S. M. 2000, ApJ, 539, 851